Nuclear "pasta" structures and the charge screening effect

Toshiki Maruyama,[1,*] Toshitaka Tatsumi,[2,†] Dmitri N. Voskresensky,[3,4,‡] Tomonori Tanigawa,[5,1,§] and Satoshi Chiba[1,¶]
[1]*Advanced Science Research Center, Japan Atomic Energy Research Institute, Tokai, Ibaraki 319-1195, Japan*
[2]*Department of Physics, Kyoto University, Kyoto, 606-8502, Japan*
[3]*Moscow Institute for Physics and Engineering, Kashirskoe sh. 31, Moscow RU-115409, Russia*
[4]*Gesellschaft für Schwerionenforschung mbH, Planckstr. 1, D-64291 Darmstadt, Germany*
[5]*Japan Society for the Promotion of Science, Tokyo 102-8471, Japan*
(Received 10 March 2005; published 21 July 2005)

Nonuniform structures of the nucleon matter at subnuclear densities are numerically studied by means of the density functional theory with relativistic mean fields coupled with the electric field. A particular role of the charge screening effects is demonstrated.

DOI: 10.1103/PhysRevC.72.015802 PACS number(s): 21.65.+f, 26.50.+x, 26.60.+c

I. INTRODUCTION

There emerged many studies of the mixed phases at various first-order phase transitions such as hadron-quark deconfinement transition [1–6], kaon condensation [7–15], color superconductivity [16–18], superfluidity in atomic traps [19], nuclear pasta [20–30], etc.

At very low densities, nuclei in matter are expected to form the Coulomb lattice embedded in the neutron-electron seas that minimizes the Coulomb interaction energy. With an increase of the density, nuclear "pasta" structures emerge [20]: the stable nuclear shape may change from droplet to rod, slab, tube, and bubble. Pasta nuclei are eventually dissolved into uniform matter at a certain nucleon density below the saturation density $\rho_0 \simeq 0.16\,\mathrm{fm}^{-3}$. Existence of pasta phases instead of the separated crystalline lattice of nuclei and the liquid *npe* phase would modify some important processes by changing the hydrodynamic properties and the neutrino opacity in supernova matter and in the matter of newly born neutron stars [31]. Also, the pasta phases may influence neutron star quakes and pulsar glitches via the change of mechanical properties of the crust matter [32].

A number of authors have investigated low-density nuclear matter using various models [20–29]. Roughly speaking, the favorable nuclear shape is determined by a balance between the surface and Coulomb energies. In most of the previous studies, the rearrangement effect of the density profile of the charged particles due to the Coulomb interaction is discarded. In Ref. [30] the electron screening effect was studied, and it was found that this effect is of minor importance. However, the rearrangement of the proton profiles as the consequence of the Coulomb repulsion was not shown in their model.

A naive application of Gibbs conditions to separate bulk phases at the first-order phase transitions, when one ignores the surface and Coulomb interaction, demonstrates a broad region of the structured mixed phase, cf. [1,8]. However, the charge screening effect (caused by the nonuniform charged particle distributions) should be very important when the typical structure size is of the order of the minimal Debye screening length in the problem. It may largely affect the stability condition of the geometrical structures in the mixed phases. We have been recently exploring the effect of charge screening in the context of the various structured mixed phases [4–6,14,15,33]. In fact, we have examined the mixed phase of the quark-hadron transition, kaon condensation, and nuclear pasta and found that in cases of the quark-hadron transition and kaon condensation the mixed phase might be largely limited by the charge screening and surface effects.

Our purpose here is, following our preliminary study [15,33], to investigate the nuclear pasta structures by means of a relativistic mean field (RMF) model, which on the one hand does not need the introduction of surface tension and on the other hand includes the Coulomb interaction in a proper way. We determine how the charge screening effects modify the results obtained disregarding these effects. In Sec. II, we formulate the model and describe our numerical procedure. In Sec. III, we demonstrate the efficiency of the model in the description of properties of finite nuclei. Then in Sec. IV, we first describe nonuniform pasta structures at a fixed proton-to-baryon number ratio that may have an application to the supernova matter and to the matter of a newly born hot protoneutron star. Then we investigate nuclear pasta at the β equilibrium, as they occur in cold neutron stars. In Sec. V, we elucidate the effects of the surface and the charge screening. Finally in Sec. VI, we arrive at our conclusions.

II. DENSITY FUNCTIONAL THEORY WITH RELATIVISTIC MEAN FIELD

A. Thermodynamic potential and equations of motion

Following the idea of the density functional theory (DFT) with the RMF model [34], we can formulate equations of motion to study nonuniform nuclear matter numerically. The RMF model with fields of mesons and baryons introduced in a Lorentz-invariant way is rather simple for numerical calculations, but realistic enough to reproduce the bulk properties of

*Electronic address: maru@hadron02.tokai.jaeri.go.jp
†Electronic address: tatsumi@ruby.scphys.kyoto-u.ac.jp
‡Electronic address: D.Voskresensky@gsi.de
§Electronic address: tanigawa@tiger02.tokai.jaeri.go.jp
¶Electronic address: sachiba@popsvr.tokai.jaeri.go.jp

nuclear matter. In our framework, the Coulomb interaction is properly included in equations of motion for nucleons, electrons, and meson mean fields, and we solve the Poisson equation for the Coulomb potential $V_{\rm Coul}$ self-consistently with them. Thus, the baryon and electron density profiles, as well as the meson mean fields, are determined in a way fully consistent with the Coulomb potential.

Note that our framework can be easily extended to other situations; for example, if we take into account kaon or pion condensations, which are likely realized in a high-density region, we should only add the relevant meson field terms. In Ref. [14], we included the kaon degree of freedom in such a treatment to discuss kaon condensation in a high-density regime.

To begin with, we present the thermodynamic potential for the system of neutrons, protons, and electrons with chemical potentials μ_a ($a = n, p, e$), respectively,

$$\Omega = \Omega_N + \Omega_M + \Omega_e, \tag{1}$$

where

$$\Omega_N = \sum_{a=p,n} \int d^3r \left[\int_0^{k_{F,a}} \frac{d^3k}{4\pi^3} \sqrt{{m_N^*}^2 + k^2} - \rho_a \nu_a \right], \tag{2}$$

with the local Fermi momenta $k_{F,a}(\mathbf{r})$ ($a = n, p$) for nucleons,

$$\Omega_M = \int d^3r \left[\frac{(\nabla\sigma)^2 + m_\sigma^2\sigma^2}{2} + U(\sigma) - \frac{(\nabla\omega_0)^2 + m_\omega^2\omega_0^2}{2} - \frac{(\nabla R_0)^2 + m_\rho^2 R_0^2}{2} \right], \tag{3}$$

for the scalar (σ) and vector mean fields (ω_0, R_0) and

$$\Omega_e = \int d^3r \left[-\frac{1}{8\pi e^2}(\nabla V_{\rm Coul})^2 - \frac{(\mu_e - V_{\rm Coul})^4}{12\pi^2} \right], \tag{4}$$

for electrons and the Coulomb potential $V_{\rm Coul}(\mathbf{r})$, where $\nu_p(\mathbf{r}) = \mu_p + V_{\rm Coul}(\mathbf{r}) - g_{\omega N}\omega_0(\mathbf{r}) - g_{\rho N} R_0(\mathbf{r})$, $\nu_n(\mathbf{r}) = \mu_n - g_{\omega N}\omega_0(\mathbf{r}) + g_{\rho N} R_0(\mathbf{r})$, $m_N^*(\mathbf{r}) = m_N - g_{\sigma N}\sigma(\mathbf{r})$, and the nonlinear potential for the scalar field $U(\sigma) = \frac{1}{3} b m_N (g_{\sigma N}\sigma)^3 + \frac{1}{4} c (g_{\sigma N}\sigma)^4$. Temperature is assumed to be zero in this study.

Here we use the local-density approximation for nucleons and electrons. Strictly speaking, the introduction of the density variable is meaningful if the typical length of the nucleon density variation inside the structure is larger than the internucleon distance. We must also bear in mind that for small structure sizes, quantum effects, which we disregard, become prominent. For the sake of simplicity, we also discard nucleon and electron density derivative terms [34]. In cases when we suppress derivative terms of nucleon densities, they follow changes of the other fields that have derivative terms. In our case, these fields are the meson mean fields and the Coulomb field. Here we consider large-size pasta structures and simply discard the density variation effect, as a first-step calculation, while it can be easily incorporated in the quasiclassical manner by the derivative expansion within the density functional theory [34]. We also could use the fact that the resulting Debye screening lengths of electrons and protons characterizing the Coulomb field profile are typically much larger than those for all meson mean fields. Then we could reduce the contribution of the latter to the surface tension term. If the nucleon (neutron and proton) length scales were shorter than those of changes of the meson mean fields, one could simplify the problem by dropping them and introducing instead a surface tension term. This simplified treatment is discussed in detail elsewhere [35]. In this paper, we avoid this simplification and solve numerically the coupled equations for the meson mean fields and the Coulomb field. Parameters of the RMF model are set to reproduce saturation properties of nuclear matter: the minimum energy per baryon -16.3 MeV at $\rho = \rho_0 = 0.153$ fm^{-3}, the incompressibility $K(\rho_0) = 240$ MeV, the effective nucleon mass $m_N^*(\rho_0) = 0.78 m_N$ with $m_N = 938$ MeV, and the symmetry energy coefficient $a_{\rm sym} = 32.5$ MeV. Coupling constants and meson masses used in our calculation are listed in Table I.

From the variational principle $\frac{\delta\Omega}{\delta\phi_i(\mathbf{r})} = 0$ ($\phi_i = \sigma, R_0, \omega_0, V_{\rm Coul}$) and $\frac{\delta\Omega}{\delta\rho_a(\mathbf{r})} = 0$ ($a = n, p, e$), we get the coupled equations of motion for the mean fields and the Coulomb potential,

$$\nabla^2\sigma(\mathbf{r}) = m_\sigma^2\sigma(\mathbf{r}) + \frac{dU}{d\sigma} - g_{\sigma N}\left[\rho_n^{(s)}(\mathbf{r}) + \rho_p^{(s)}(\mathbf{r})\right], \tag{5}$$

$$\nabla^2\omega_0(\mathbf{r}) = m_\omega^2\omega_0(\mathbf{r}) - g_{\omega N}[\rho_p(\mathbf{r}) + \rho_n(\mathbf{r})], \tag{6}$$

$$\nabla^2 R_0(\mathbf{r}) = m_\rho^2 R_0(\mathbf{r}) - g_{\rho N}[\rho_p(\mathbf{r}) - \rho_n(\mathbf{r})], \tag{7}$$

$$\nabla^2 V_{\rm Coul}(\mathbf{r}) = 4\pi e^2 \rho_{\rm ch}(\mathbf{r}), \tag{8}$$

with the scalar densities $\rho_a^{(s)}(\mathbf{r})$ ($a = n, p$), and the charge density $\rho_{\rm ch}(\mathbf{r}) = \rho_p(\mathbf{r}) + \rho_e(\mathbf{r})$. Equations of motion for fermions yield the standard relations between the densities and chemical potentials,

$$\mu_n = \mu_B = \sqrt{k_{F,n}^2(\mathbf{r}) + m_N^*(\mathbf{r})^2} + g_{\omega N}\omega_0(\mathbf{r}) - g_{\rho N} R_0(\mathbf{r}), \tag{9}$$

$$\mu_p = \mu_B - \mu_e = \sqrt{k_{F,p}^2(\mathbf{r}) + m_N^*(\mathbf{r})^2} + g_{\omega N}\omega_0(\mathbf{r}) + g_{\rho N} R_0(\mathbf{r}) - V_{\rm Coul}(\mathbf{r}), \tag{10}$$

$$\rho_e(\mathbf{r}) = -[\mu_e - V_{\rm Coul}(\mathbf{r})]^3/3\pi^2, \tag{11}$$

where we have assumed that the system is in chemical equilibrium among nucleons and electrons and introduced the baryon number chemical potential μ_B and the electron number chemical potential μ_e. Note that first, the Poisson equation for

TABLE I. Parameter set used in RMF in our calculation.

$g_{\sigma N}$	$g_{\omega N}$	$g_{\rho N}$	b	c	m_σ (MeV)	m_ω (MeV)	m_ρ (MeV)
6.3935	8.7207	4.2696	0.008659	0.002421	400	783	769

the Coulomb field (8) is highly nonlinear in $V_{\rm Coul}(\mathbf{r})$, since $\rho_{\rm ch}(\mathbf{r})$ in the right-hand side includes it in a complicated way. The Coulomb potential always enters equations through the gauge invariant combinations $\mu_e - V_{\rm Coul}(\mathbf{r})$ and $\mu_p + V_{\rm Coul}(\mathbf{r})$.

B. Numerical procedure

To solve the above coupled equations numerically, we use the Wigner-Seitz cell approximation: the whole space is divided into equivalent cells with a geometry. The geometrical shape of the cell changes: sphere in three-dimensional (3D) calculation, cylinder in 2D, and slab in 1D. Each cell is globally charge neutral, and all the physical quantities in a cell are smoothly connected to those of the next cell with zero gradients at the boundary. Every point inside the cell is represented by the grid point ($N_{\rm grid} \approx 100$), and the differential equations for fields are solved by the relaxation method for a given baryon number density under the constraint of the global charge neutrality.

To illustrate how to numerically solve equations of motion for the mean fields, let us consider, for simplicity, two fields $f_1(r)$, $f_2(r)$ and their coupled Poisson-like equations under 3D calculation,

$$\begin{aligned} \nabla^2 f_1(r) &= {m_1}^2 f_1(r) + W_1[f_1, f_2], \\ \nabla^2 f_2(r) &= {m_2}^2 f_2(r) + W_2[f_1, f_2], \end{aligned} \tag{12}$$

where W_i $(i = 1, 2)$ are functions of the fields f_1 and f_2. Introducing a relaxation "time" t artificially, we solve the equation,

$$\frac{\partial f_i(r;t)}{\partial t} = c_i(\nabla^2 f_i(r;t) - m^2 f_i(r;t) - W_i[f_1, f_2]). \tag{13}$$

If the coefficients c_i are appropriately chosen, the above $f_i(r;t)$ will converge to be constant in time and we get the solution of Eq. (12).

The profiles of the nucleon densities are solved with the help of the "local chemical potentials" $\mu_a(r)$ $(a = n, p)$, which are different from the constant chemical potentials which we initially introduced. Assuming $\mu_a(r)$ is an increasing function of the neutron or proton number density $\rho_a(r)$ in Eqs. (9) and (10), the relaxation equation for the neutron or proton density profile,

$$\frac{\partial \rho_a(r;t)}{\partial t} = c_a(r;t)\rho_a(r;t)\nabla^2\mu_a(r;t), \tag{14}$$

is solved to get rid of the spatial dependence of the local chemical potentials $\mu_a(r;t)$. The coefficients $c_a(r;t)$ $(a = n, p)$ are not constant so as to conserve the total proton and neutron numbers. When we impose the β equilibrium condition, proton and neutron densities are adjusted to achieve $\mu_n(r) = \mu_p(r) + \mu_e(r)$. Finally we get the density profiles $\rho_n(r)$ and $\rho_p(r)$ relating to the constant chemical potentials $\mu_n(r) = \mu_n$ and $\mu_p(r) = \mu_p$. Although the basic idea is to attain the constant chemical potentials $\mu_a(r) = \mu_a$ $(a = n, p)$ at the convergence, there is an exception: in regions where $\rho_a(r) = 0$, the local chemical potentials $\mu_a(r)$ are larger than the constant value in the regions where $\rho_a(r) \neq 0$.

The electron density profile $\rho_e(r)$ is calculated directly from Eq. (11). The value of μ_e is adjusted at any time step to maintain the global charge neutrality: we decrease μ_e when the total charge in a cell is positive and increase when it is negative.

All the above relaxation procedures are performed simultaneously.

III. BULK PROPERTIES OF FINITE NUCLEI

Before applying our framework to the problem of the pasta phase in nucleon matter, let us check how well it works in describing finite nuclei. In this calculation, for simplicity, we assume the spherical shape of nuclei. The electron density is set to zero. Therefore, neither the global charge neutrality condition nor the local charge-neutrality condition is imposed.

In Fig. 1 (left panel) we show the density profiles of some typical nuclei. One can see how well our framework may reproduce the density profiles. To obtain a still better fit, especially around the surface region, we might need to include the derivative terms of the nucleon densities, as we have already remarked. Fine structures seen in the empirical density profiles, which may come from the shell effects (see,

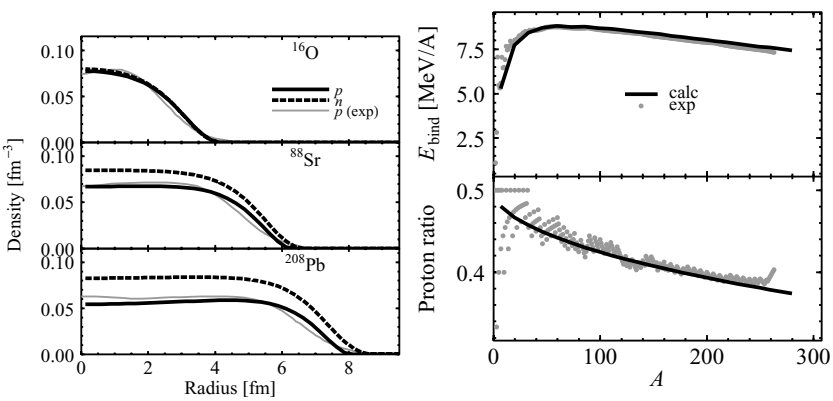

FIG. 1. Properties of finite nuclei obtained with the present RMF model. Left: density profiles of typical nuclei. Proton number densities (solid curves) are compared with the experiment. Right: binding energy per nucleon and proton number ratio of finite nuclei.

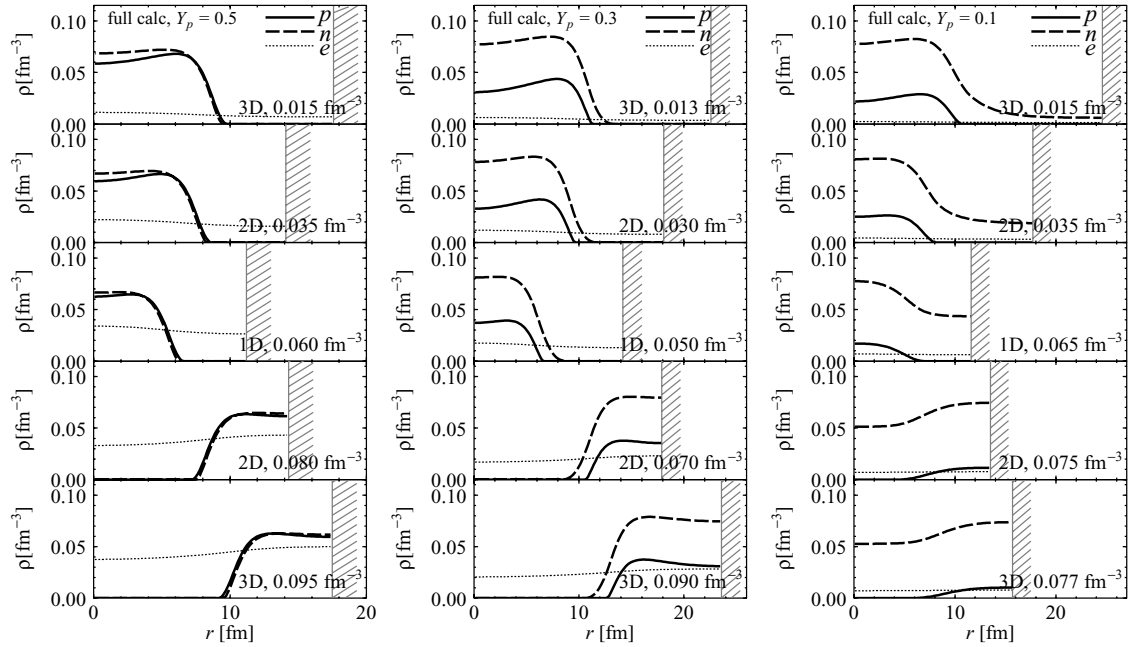

FIG. 2. Examples of the density profiles in the cell for symmetric nuclear matter with $Y_p = 0.5$ (left panel) and for asymmetric matter with $Y_p = 0.3$ (center panel) and 0.1 (right panel).

e.g., a proton density dip at the center of a light ^{16}O nucleus), cannot be reproduced by the mean-field theory. The effect of the rearrangement of the proton density distribution is seen in heavy nuclei. Protons repel each other, which enhances their contamination near the surface of heavy nuclei. This effect is analogous to the charge screening effect for the Coulomb potential in the sense that the proton distribution is now changed not on the scale of the nuclear radius but on another length scale, which we will call the proton Debye screening length [see Eq. (16) below]. It gives rise to important consequences for the pasta structures since typically the proton Debye screening length is less than the droplet size. The optimal value of the proton Z to the total baryon A number ratio $Y_p = Z/A$ is obtained by imposing the β equilibrium condition for a given baryon number. Figure 1 (right panel) shows the baryon number dependence of the binding energy per baryon and the proton number ratio. We can see that the bulk properties of finite nuclei (density, binding energy, and proton-to-baryon number ratio) are satisfactorily reproduced for our present purpose.

Note that in our framework we must use a sigma mass $m_\sigma = 400$ MeV [36], a slightly smaller value than usually used, to get an appropriate fit. If we used a popular value $m_\sigma \approx 500$ MeV, finite nuclei would be overbound by about 3 MeV/A. The actual value of the sigma mass (as well as the omega and rho masses) has little relevance for the case of infinite nucleon matter, since it enters the thermodynamic potential only in the combination $\widetilde{C}_\sigma = g_{\sigma N}/m_\sigma$. However, meson masses are important characteristics of finite nuclei and of other nonuniform nucleon systems, such as those in pasta. The effective meson mass characterizes the typical scale for the spatial change of the meson field, and consequently it affects the value of the effective surface tension [35].

IV. NONUNIFORM STRUCTURES IN NUCLEON MATTER

A. Nucleon matter at fixed proton number ratios

First, we are concentrated on the discussion of the behavior of the nucleon matter at a fixed value of the proton number ratio Y_p. Particularly, we explore the proton number ratios $Y_p = 0.1$, 0.3, and 0.5. The cases $Y_p = 0.3$–0.5 should be relevant for the supernova matter and for newly born neutron stars. Figure 2 shows some typical density profiles inside the Wigner-Seitz cells. The geometrical dimension of the cell is denoted as 3D (three-dimensional sphere), etc. The horizontal axis in each panel denotes the radial distance from the center of the cell. The cell boundary is indicated by the hatch. From top to bottom, the configuration corresponds to droplet (3D), rod (2D), slab (1D), tube (2D), and bubble (3D). The nuclear pasta structures are clearly manifested. For the lowest Y_p case ($Y_p = 0.1$), the neutron density is finite at any point: the space is filled by dripped neutrons. The neutron-drip value of Y_p is around 0.26 in our 3D calculation, for example. For a higher Y_p, the neutron density drops to zero outside the nucleus. The proton number density always drops to zero outside the nucleus. We can see that the charge screening effects are pronounced. Due to the spatial rearrangement of electrons, the electron density profile becomes no more uniform. This nonuniformity of the electron distribution is more pronounced for a higher Y_p and a higher density. Protons repel each other. Thereby the proton density profile substantially deviates from the step function. The proton number density is enhanced near the surface of the nucleus.

The equation of state (EOS) for the sequence of geometric structures is shown in Fig. 3 (top panels) as a function of the averaged baryon number density. Note that the energy $E - m_N$ also includes the kinetic energy of electrons,

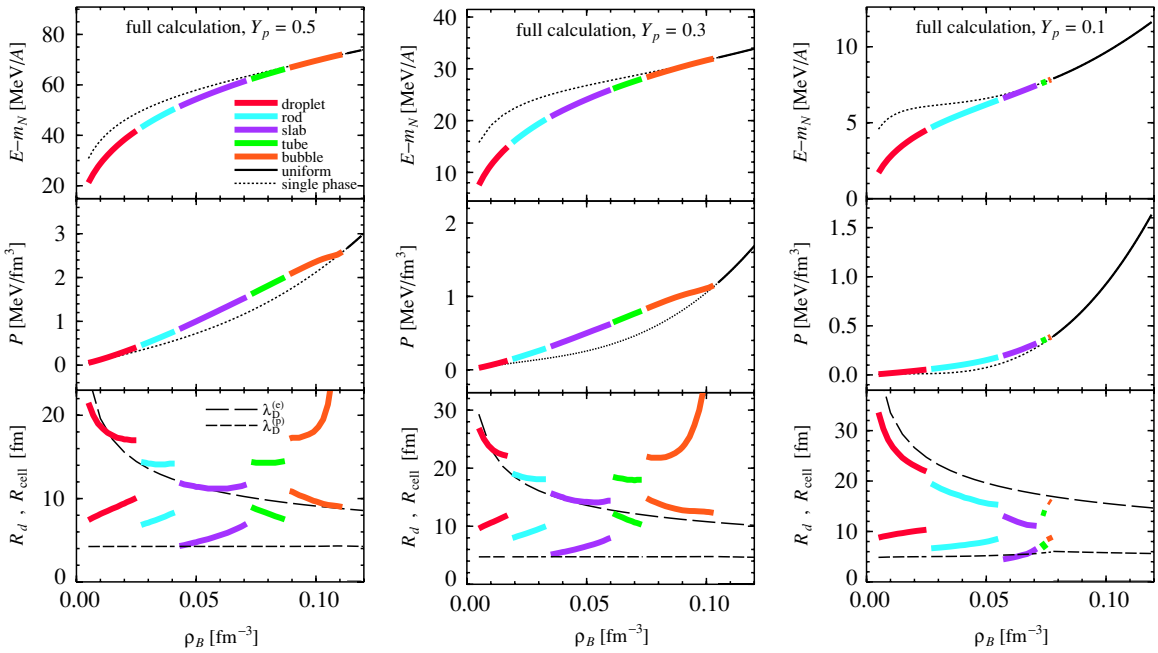

FIG. 3. (Color online) Binding energy per nucleon, pressure, and cell and nuclear sizes for symmetric nuclear matter with $Y_p = 0.5$ (left panel), and for asymmetric matter with $Y_p = 0.3$ (center panel) and 0.1 (right panel).

which makes the total pressure positive (middle panels). The lowest-energy configurations are selected among various geometrical structures. The most favorable configuration changes from the droplet to rod, slab, tube, bubble, and to the uniform one (the dotted thin curve) with an increase of density. The appearance of nonuniform structures in matter results in a softening of EOS: the energy per baryon gets lower up to about 15 MeV/A compared to the uniform matter.

The bottom panels in Fig. 3 are the cell radii $R_{\rm cell}$ and nuclear radii R_d versus averaged baryon number density. The radius R_d is defined by way of a density fluctuation as

$$R_d = \begin{cases} R_{\rm cell}\dfrac{\langle\rho_p\rangle^2}{\langle\rho_p^2\rangle}, & \text{(for droplet, rod, and slab)} \\ R_{\rm cell}\left(1-\dfrac{\langle\rho_p\rangle^2}{\langle\rho_p^2\rangle}\right), & \text{(for tube and bubble),} \end{cases} \tag{15}$$

where the bracket "$\langle\,\rangle$" indicates the average along the radial (for 3D and 2D cases) or perpendicular (1D) direction in the cell. Dashed curves show the Debye screening lengths of electron and proton calculated as

$$\lambda_D^{(e)} = \left(-4\pi e^2\frac{d\rho_e^{\rm av}}{d\mu_e}\right)^{-1/2}, \tag{16}$$

$$\lambda_D^{(p)} = \left(4\pi e^2\frac{d\rho_p^{\rm av}}{d\mu_p}\right)^{-1/2}, \tag{17}$$

where $\rho_p^{\rm av}$ is the proton number density averaged inside the nucleus (the region with finite ρ_p) and $\rho_e^{\rm av}$ is the electron charge density averaged inside the cell. Actually, to do this more carefully, we should introduce four Debye screening lengths $\lambda_D^{(a,<)}$ and $\lambda_D^{(a,>)}$ with a separate averaging for the interior and the exterior of the nuclei. However, we observe that the proton number density is always zero in the exterior region, and thereby $\lambda_D^{(p,>)} = \infty$. Electrons $\lambda_D^{(e,<)}$ and $\lambda_D^{(e,>)}$ are in general different but both are large and of the same order of magnitude in the pasta case under consideration. Therefore, we actually do not need a more detailed analysis of these quantities. Note that these values are obviously gauge invariant. Numerically, the cell radii $R_{\rm cell}$ for droplet, rod, and slab configurations at $Y_p = 0.5$ and 0.3 were proven to be close to the electron screening length. For the tube, $R_{\rm cell}$ is larger than $\lambda_D^{(e)}$. For $Y_p = 0.1$, in all cases $R_{\rm cell}$ is substantially smaller than $\lambda_D^{(e)}$, and thus the electron screening should be much weaker. In all cases, except for bubbles (at $Y_p = 0.5$ and 0.3), the structure radii R_d are smaller than $\lambda_D^{(e)}$. This means that the Debye screening effect of electrons inside these structures should not be pronounced. For bubbles at $Y_p = 0.5$ and 0.3, $\lambda_D^{(e)}$ is substantially smaller than the cell size and the electron screening should be significant (see Fig. 9 below). For $Y_p = 0.5$, 0.3, 0.1 in all cases (with the only exception $Y_p = 0.1$ for slabs), the value $\lambda_D^{(p,<)}$ is shorter than R_d. Hence, the density rearrangement of protons is essential for the pasta structures, as it is indeed seen from Fig. 2.

Using the baryon number density and nuclear radius from Fig. 3, one may estimate the atomic number of the nucleus. In the case of droplets and for $Y_p = 0.5$, the atomic number of the droplet is $\simeq$25 in the low-density limit and $\simeq$65 at the maximum density of the droplet phase $\rho_{B,d}^{(\rm max)} \simeq 0.025\,{\rm fm}^{-3}$.

B. Nucleon matter in β equilibrium

Next, we consider the neutron star matter at zero temperature and explore the nonuniform structures for the nucleon

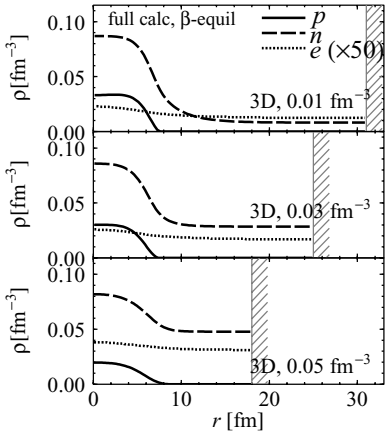

FIG. 4. Density profiles in the cell for nuclear matter in β equilibrium with baryon number densities 0.01, 0.03, and 0.05 fm^{-3}.

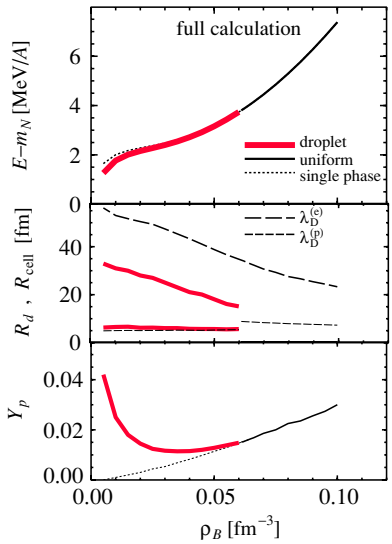

FIG. 5. (Color online) Binding energy (top), cell and nuclear sizes (middle), and proton number ratio (bottom) in the cell for nuclear matter in β equilibrium.

matter in β equilibrium. Figure 4 shows the density profiles for different baryon number densities. The droplet structure itself is quite similar to the case of the fixed proton number ratio $Y_p = 0.1$ considered above. The apparently different feature in this case is that only the droplet configuration appears as a nonuniform structure. It should be noticed, however, that the presence or absence of the concrete pasta structure sensitively depends on the choice of the effective interaction.

In Fig. 5, we plot the energy per baryon (top), the cell and nuclear sizes (middle), and the proton number ratio (bottom). The effect of the non-uniform structure on EOS (the difference between the energy of uniform matter and that of non-uniform one) is small. However, the proton number ratio is significantly affected by the presence of the pasta at lower densities. In the zero-density limit, the proton number ratio should converge to that of the normal nuclei. The droplet radius and cell radius in the middle panel of Fig. 5 are always smaller than the electron Debye screening length $\lambda_D^{(e)}$. Thereby, the effect of the electron charge screening is small. Unlike the fixed Y_p cases, the droplet radius is comparable to the proton Debye screening length, which means that the effect of the proton rearrangement is not pronounced in this case. In fact, there is no enhancement of the proton number density near the surface in Fig. 4, in contrast to that in Fig. 2.

It would be useful for further applications to present a table containing the subnuclear EOS in β equilibrium. To this end, Table II shows pressure, energy density, and proton number fraction versus baryon number density.

V. COMPARISON WITH OTHER CALCULATIONS

In this section, we compare our DFT calculation with others to explore the effects of the surface, the charge rearrangement, and the fully consistent treatment of the density distribution.

TABLE II. EOS of matter in β equilibrium. Pressure P, energy density $\epsilon - m_N\rho_B$, and proton number ratio Y_p are listed for baryon number density ρ_B.

ρ_B (fm^{-3})	P (MeV/fm^3)	$\epsilon - m_N\rho_B$ (MeV/fm^3)	Y_p	ρ_B (fm^{-3})	P (MeV/fm^3)	$\epsilon - m_N\rho_B$ (MeV/fm^3)	Y_p
	Droplet				Uniform		
0.005	0.0039483	0.0063025	0.042926	0.061	0.2418000	0.2319342	0.015024
0.010	0.0065066	0.0176880	0.025492	0.065	0.2989100	0.2647905	0.016435
0.015	0.0080088	0.0301290	0.018096	0.070	0.3813600	0.3111640	0.018241
0.020	0.0100940	0.0431160	0.014486	0.075	0.4767400	0.3638775	0.020093
0.025	0.0147800	0.0568900	0.012485	0.080	0.5856100	0.4233920	0.021986
0.030	0.0236970	0.0719850	0.011608	0.085	0.7085500	0.4901440	0.023914
0.035	0.0383230	0.0890085	0.011340	0.090	0.8460400	0.5645520	0.025874
0.040	0.0599000	0.1085920	0.011497	0.095	0.9985700	0.6470070	0.027863
0.045	0.0896340	0.1313550	0.011926	0.100	1.1666000	0.7379000	0.029877
0.050	0.1280100	0.1578800	0.012708				
0.055	0.1756500	0.1886940	0.013734				
0.060	0.2313900	0.2242440	0.014902				

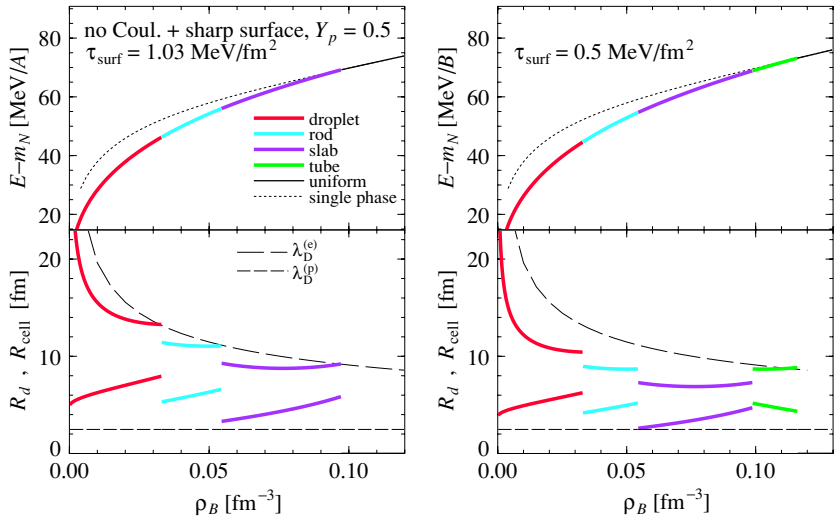

FIG. 6. (Color online) Bulk calculations with the surface tension parameter $\tau_{surf} = 1.03$ and 0.5 MeV/fm^2.

First let us focus on a very simplified treatment that has been used in the literature. We consider the bulk calculation supplemented by a simplified treatment of the finite-size effect. For description of the latter, we introduce the surface tension and a bare (nonscreened) Coulomb interaction. This calculation assumes a sharp boundary between dense and dilute phases, uniform baryon density distribution inside each phase, and uniform electron density distribution all over the cell. To further specify this approximation, we use the term "no Coulomb + sharp surface." We totally discard the Coulomb potential in equations of motion and drop the Poisson equation ("no Coulomb") and we reduce the mean fields to their constant bulk values in the interior and the exterior of the structure ("+sharp surface"). The Coulomb energy, evaluated with the step-function-like density profiles, and the surface energy, expressed via the surface tension parameter τ_{surf}, are added to the total bulk energy.

The volume fraction of each phase is simply calculated without taking into account the finite-size effect ("bulk calculation"). Details of the "no Coulomb + sharp surface" calculation are presented in Appendix A.

Figure 6 shows the EOS obtained by the "no Coulomb + sharp surface" calculation performed at different values of the surface tension. In this case for $Y_p = 0.5$, the dilute phase includes no baryon. The value of the surface tension parameter $\tau_{surf} \simeq 1.03$ MeV/fm^2 fits the liquid-drop binding energies of finite nuclei. Note that the appearance or disappearance of the pasta structure essentially depends on the value of the surface tension. With a larger value of the surface tension, the density region of the pasta structure reduces and even some of the structures, e.g., "tube" and "bubble," disappear. With a smaller value of the surface tension, the region of the pasta structure broadens and all kinds of pasta structures appear if we take $\tau_{surf} \leqslant 0.3$ MeV/fm^2. However, if we put the surface tension at zero, the mixed phase develops from zero to the saturation density ρ_0 without any specific geometry. Therefore, from the given example we see that the surface tension plays a crucial role in the appearance of pasta structures. Remember that in the case under consideration, the pasta structures are realized by a balance of the surface tension and the bare Coulomb interaction, which reads $E_{surf} = 2E_{Coul}$, where E_{surf} is the surface energy and E_{Coul} the bare Coulomb energy. Therefore, the Coulomb interaction is important as well. Please also note that the surface tension introduced here simulates effects of the spatial changes of the meson mean fields. In our "full calculation," the latter effects are taken into account explicitly, whereas purely "bulk calculations" completely disregard these effects.

Next we compare three kinds of calculations with different treatments of the Coulomb interaction. One is the "full calculation" which we have done here. The second is the calculation that disregards electron screening ("no e-screening"): a constraint is used that the electron density should be uniform. In this calculation, the Coulomb potential V_{Coul} in Eq. (11) is replaced by a constant $V_0 = 0$,

$$\rho_e = -(\mu_e - V_0)^3/3\pi^2. \tag{18}$$

In the full calculation, the value of V_0 is arbitrary, and one can take V_0 for the sake of convenience, e.g., as $V_0 = 0$, or set it equal to the averaged value of $V_{Coul}(r)$ over the cell: recall that V_{Coul} or μ_e alone does not have a physical meaning but only the combination $\mu_e - V_{Coul}$ is meaningful because of the gauge invariance, cf. [4,5]. However, in the case of no e-screening, the gauge invariance is violated as seen in Eq. (10), since we replace V_{Coul} to $V_0 = 0$ in the equation for the electron chemical potential but retain V_{Coul} in the equation for the proton chemical potential and thus in the expression for the proton number density. We do this procedure just to demonstrate the efficiency of the proton rearrangement while artificially suppressing that of the electron one. The third calculation, called "no Coulomb," is performed by totally discarding the Coulomb potential V_{Coul} in equations of motion. Accordingly, the Poisson equation is discarded as well. After obtaining the density profiles, the Coulomb energy, being evaluated using charge densities thus determined, is added to the total energy. This calculation is similar to the no Coulomb + sharp surface calculation discussed above. The difference is that the effect of the density variation near the structure surface is automatically incorporated in the no Coulomb calculation,

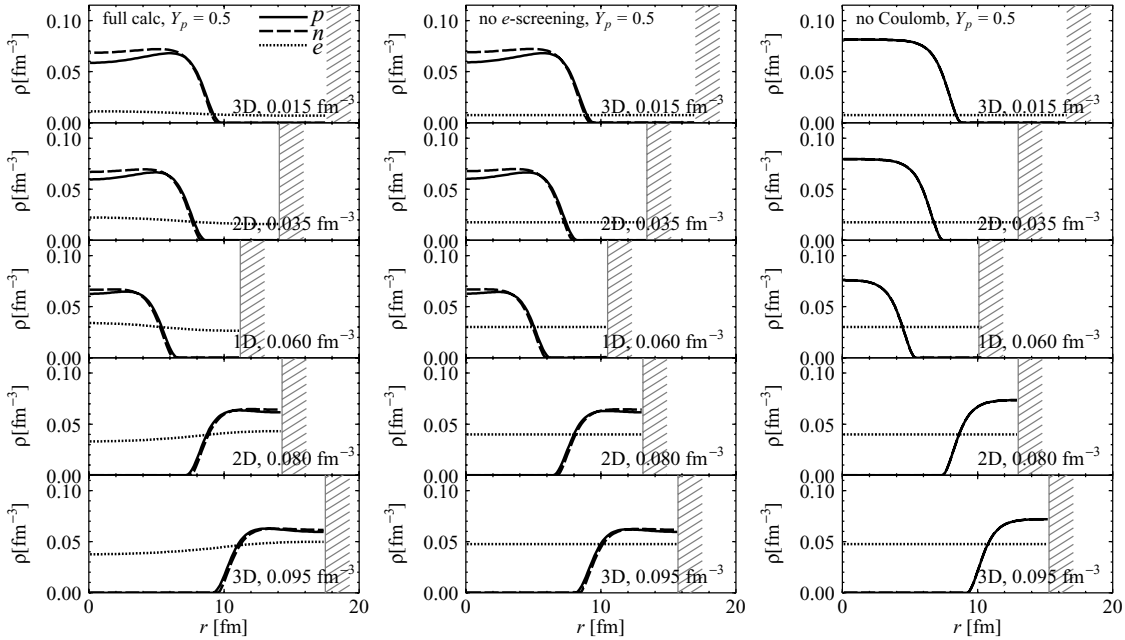

FIG. 7. Comparison of the density profiles for different treatments of the Coulomb interaction. From the left: full calculation, without electron screening, and "no Coulomb" calculation. The proton number ratio $Y_p = 0.5$ for all cases.

while in the no Coulomb + sharp surface calculation this effect is hidden in the value of the surface tension.

In Fig. 7, the density profiles are compared for different treatments of the Coulomb interaction. The left panel is the same as that in Fig. 2. It demonstrates the full calculation. It seems that there is almost no difference between the nucleon density of the full calculation and that of the no e-screening calculation (center). The case of no Coulomb calculation (right), however, shows a significant difference, especially in the proton number density. The reason is simple: the electron Debye screening length is large, whereas the proton Debye screening length is rather short. Thus the proton screening effects are much more pronounced than the electron ones.

The EOS as a whole (upper panels in Fig. 8) shows almost no dependence on the treatments of the Coulomb interaction. This agrees with a general statement that the variational functional is always less sensitive to the choice of the trial functions than the quantities linearly depending on them. Nevertheless, sizes of the cell and the nucleus (lower panels in Fig. 8) especially for tube and bubbles are different. In the cases of the full calculation and no e-screening, the cell radii of tube, bubble and slab structures at the higher-density side get larger with an increase of density, while they are monotonically decreasing in the no Coulomb calculation. We see almost no difference between the full and no e-screening calculations, which again demonstrates the weakness of the

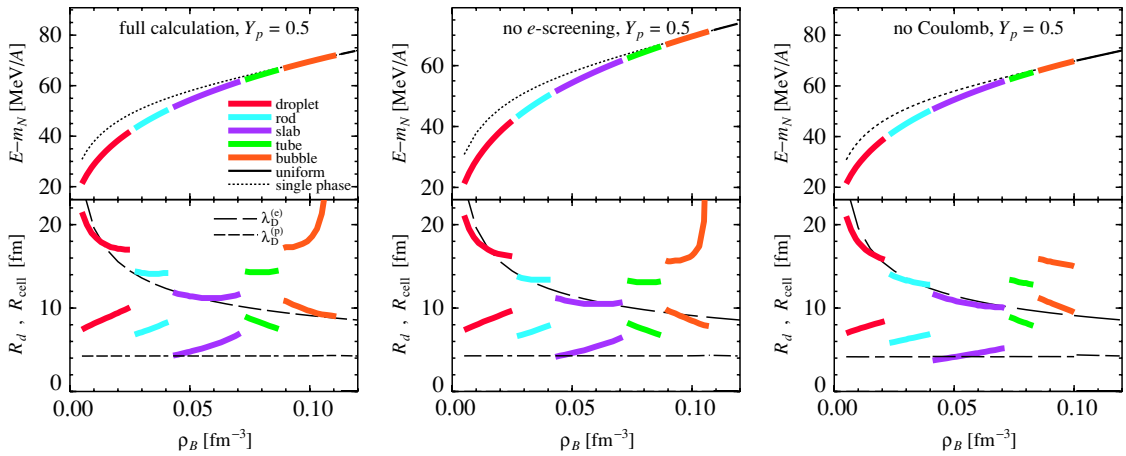

FIG. 8. (Color online) Comparison of the density profiles for different treatments of the Coulomb interaction. From the left: "full" calculation, "no electron screening", and "no Coulomb" calculation. The proton number ratio is $Y_p = 0.5$ for all cases.

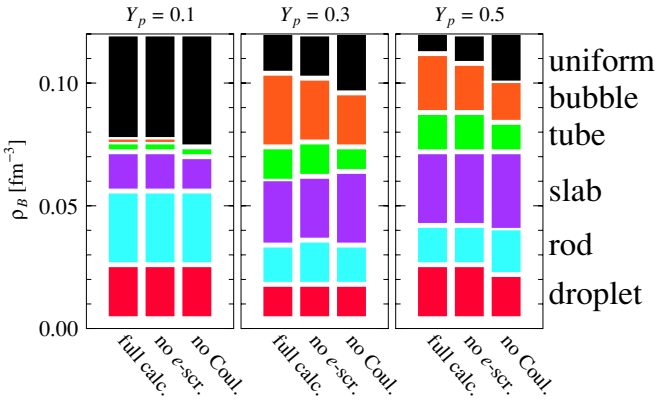

FIG. 9. (Color online) Comparison of the phase diagrams between different treatments of the Coulomb interaction.

electron screening effects. The most significant point seen in Fig. 9 is the disappearance of the bubble structure in the no Coulomb calculation for $Y_p = 0.1$. The other effect is a difference in the density range for each pasta structure. The full treatment of the Coulomb interaction slightly increases the region of the nuclear pasta. For $Y_p = 0.1$, the differences between full and no e-screening calculations are completely eliminated.

VI. SUMMARY AND CONCLUDING REMARKS

We have discussed the low-density nuclear matter structures called nuclear pasta and elucidated the charge screening effect. Using a self-consistent framework based on density functional theory and relativistic mean fields, we took into account the Coulomb interaction in a proper way and numerically solved the coupled equations of motion to extract the density profiles of nucleons.

First we checked how realistic our framework is by calculating the bulk properties of finite nuclei, as well as the saturation properties of nuclear matter, and found that it can describe both features satisfactorily. One could still improve the consideration fitting other experimental data. For example, we could more carefully fit different terms in the Weiczecker equation such as the surface energy and the shell terms. For that we might need an improvement of our relativistic mean-field model that does not include the gradient terms of proton and neutron densities.

In isospin-asymmetric nuclear matter for fixed proton-to-baryon number ratios, we have observed the nuclear pasta structures with various geometries at subnuclear densities. These cases are relevant to the discussion of supernova explosions and the description of newly born neutron stars. The appearance of pasta structures significantly lowers the energy, i.e., softens the equation of state, while the energy differences between various geometrical structures are rather small. The spatial rearrangement of the proton and electron charge densities (screening) affect the geometrical structures.

By comparing different treatments of the Coulomb interaction, we have seen that the self-consistent inclusion of the Coulomb interaction changes the phase diagram. In particular, the region of the pasta structure is broader for a full calculation compared to that with simplified treatments of the Coulomb interaction, which have been used in previous studies. The effect of the rearrangement of the proton distributions on the structures is much more pronounced compared to the effect of the electron charge screening. The influence of charge screening on the equation of state, on the other hand, was found to be small.

We also studied the structure of nucleon matter in the β equilibrium. We found that only one type of structure is realized: proton-enriched droplets embedded in the neutron sea. No other geometrical structures such as rod, slab, etc., appeared.

In our calculation, the transition between pasta structures occurs suddenly as the baryon number density changes. This situation may not be realistic. At the transient region between two different structures, a kind of complex and intermediate structure may appear. Such a situation is also relevant to the dynamical (time-dependent) change of density. In Ref. [37], transition of pasta structures during compression of supernova matter was demonstrated by a molecular dynamics simulation. During the transition, complex and intermediate structures, e.g., a spongelike structure between a rod and a slab, were observed in the simulation. We expect, however, that such intermediate structures do not affect the EOS of matter since the energy difference is very small between different pasta structures.

In application to newly formed neutron stars, as in supernova explosions, finite temperature and neutrino trapping effects become important, as well as the dynamics of the first order phase transition with formation of the structures. It would be interesting to extend our framework to include these effects.

ACKNOWLEDGMENTS

This work is partially supported by the Grant-in-Aid for the 21st Century COE "Center for the Diversity and Universality in Physics" from the Ministry of Education, Culture, Sports, Science and Technology of Japan. It is also partially supported by the Japanese Grant-in-Aid for Scientific Research Fund of the Ministry of Education, Culture, Sports, Science and Technology (13640282, 16540246). The work of D.N.V. was also supported in part by the Deutsche Forschungsgemeinschaft (DFG Project 436 RUS 113/558/0-2).

APPENDIX A: "BULK" AND "NO COULOMB + SHARP SURFACE" CALCULATION OF LOW-DENSITY NUCLEON MATTER

The bulk calculation proceeds like this [2,3,7,16,20]: first consider two semi-infinite matters, (I) dense and (II) dilute phases, with a sharp boundary. The Coulomb and surface interactions are discarded for now. Conditions of thermal equilibrium at zero temperature are imposed for pressure P

and chemical potential μ_a ($a = n, p$) between the two phases:

$$\begin{aligned} P^{(\mathrm{I})} &= P^{(\mathrm{II})}, \\ \mu_p^{(\mathrm{I})} &= \mu_p^{(\mathrm{II})}, \\ \mu_n^{(\mathrm{I})} &= \mu_n^{(\mathrm{II})}. \end{aligned} \tag{A1}$$

In Sec. IV A, the case is considered when the β equilibrium is not imposed but the proton-to-baryon number ratio Y_p is fixed.

The averaged densities are $\rho_p = f\rho_p^{(\mathrm{I})} + (1-f)\rho_p^{(\mathrm{II})}$ and $\rho_n = f\rho_n^{(\mathrm{I})} + (1-f)\rho_n^{(\mathrm{II})}$. Here f is the volume fraction of phase (I). The chemical potentials are calculated using the RMF model presented in this paper. Taking into account the above conditions (A1), we obtain a set of $\rho_n^{(\mathrm{I})}$, $\rho_n^{(\mathrm{II})}$, $\rho_p^{(\mathrm{I})}$, $\rho_p^{(\mathrm{II})}$, $P^{(\mathrm{I})} = P^{(\mathrm{II})}$, f, and the bulk energy density ϵ_{bulk} in each phase for given ρ_n and ρ_p. At this point ϵ_{bulk} does not include the surface and Coulomb contributions. If one cannot find the solution with finite $\rho_n^{(\mathrm{II})}$ and $\rho_p^{(\mathrm{II})}$, the proton or neutron density of the dilute phase is set to zero. In this case the corresponding chemical potential is larger in phase (II) than in phase (I), and the complete set of the Gibbs conditions is not fulfilled.

Now let us specify the no Coulomb + sharp surface calculation. To consider the structure of the mixed phase, the balance between the Coulomb and surface interactions should be taken into account. Introducing an adjusting parameter of the surface tension τ_{surf}, we calculate the surface energy density for the given geometrical dimension D as

$$\epsilon_{\mathrm{surf}} = \frac{\tau_{\mathrm{surf}} f D}{R_d}, \tag{A2}$$

where R_d is the droplet radius. The Coulomb energy density can be calculated [20] as

$$\epsilon_{\mathrm{Coul}} = 2\pi e^2 \left(\rho_p^{(\mathrm{I})} - \rho_p^{(\mathrm{II})}\right)^2 {R_d}^2 f \Phi, \tag{A3}$$

$$\Phi \equiv \left[\frac{2 - D f^{1-2/D}}{D-2} + f\right] \frac{1}{D+2}. \tag{A4}$$

By minimizing $\epsilon_{\mathrm{surf}} + \epsilon_{\mathrm{Coul}}$ in R_d (the relation $\epsilon_{\mathrm{surf}} = 2\epsilon_{\mathrm{Coul}}$), we get

$$R_d = \left[\frac{\tau_{\mathrm{surf}} D}{4\pi \left(\rho_p^{(\mathrm{I})} - \rho_p^{(\mathrm{II})}\right)^2 \Phi}\right]^{1/3}, \tag{A5}$$

$$\epsilon_{\mathrm{Coul}} + \epsilon_{\mathrm{surf}} = 3 f D \left[\frac{\pi \tau_{\mathrm{surf}}^2 \left(\rho_p^{(\mathrm{I})} - \rho_p^{(\mathrm{II})}\right)^2 \Phi}{2D}\right]^{1/3}. \tag{A6}$$

Comparing the energy density of the uniform matter ε and those of mixed phases $\epsilon_{\mathrm{bulk}} + \epsilon_{\mathrm{surf}} + \epsilon_{\mathrm{Coul}}$ with different geometrical dimension D, we can determine the most favorable configuration and its energy density.

[1] N. K. Glendenning, Phys. Rev. D **46**, 1274 (1992); Phys. Rep. **342**, 393 (2001).
[2] H. Heiselberg, C. J. Pethick, and E. F. Staubo, Phys. Rev. Lett. **70**, 1355 (1993).
[3] N. K. Glendenning and S. Pei, Phys. Rev. C **52**, 2250 (1995).
[4] D. N. Voskresensky, M. Yasuhira, and T. Tatsumi, Phys. Lett. **B541**, 93 (2002); T. Tatsumi and D. N. Voskresensky, *Proceedings of the International Symposium on the Origin of Matter and Evolution of Galaxies 2003*, edited by M. Terasawa *et al*., (World Scientific, Singapore, 2005), p. 397.
[5] D. N. Voskresensky, M. Yasuhira, and T. Tatsumi, Nucl. Phys. **A723**, 291 (2003).
[6] T. Endo, Toshiki Maruyama, S. Chiba, and T. Tatsumi, Nucl. Phys. **A749**, 333 (2005).
[7] N. K. Glendenning and J. Schaffner-Bielich, Phys. Rev. C **60**, 025803 (1999).
[8] M. B. Christiansen and N. K. Glendenning, astro-ph/0008207.
[9] M. B. Christiansen, N. K. Glendenning, and J. Schaffner-Bielich, Phys. Rev. C **62**, 025804 (2000).
[10] J. A. Pons, S. Reddy, P. J. Ellis, M. Prakash, and J. M. Lattimer, Phys. Rev. C **62**, 035803 (2000).
[11] M. Yasuhira and T. Tatsumi, Nucl. Phys. **A690**, 769 (2001).
[12] S. Reddy, G. Bertsch, and M. Prakash, Phys. Lett. **B475**, 1 (2000).
[13] T. Norsen and S. Reddy, Phys. Rev. C **63**, 065804 (2001).
[14] Toshiki Maruyama, T. Tatsumi, D. N. Voskresensky, T. Tanigawa, and S. Chiba, Nucl. Phys. **A749**, 186 (2005).
[15] T. Tatsumi, Toshiki Maruyama, D. N. Voskresensky, T. Tanigawa, and S. Chiba, nucl-th/0502040.
[16] M. Alford, K. Rajagopal, S. Reddy, and F. Wilczek, Phys. Rev. D **64**, 074017 (2001).
[17] P. F. Bedaque, Nucl. Phys. **A697**, 569 (2002).
[18] S. Reddy and G. Rupak, Phys. Rev. C **71**, 025201 (2005).
[19] P. F. Bedaque, H. Caldas, and G. Rupak, Phys. Rev. Lett. **91**, 247002 (2003).
[20] D. G. Ravenhall, C. J. Pethick, and J. R. Wilson, Phys. Rev. Lett. **50**, 2066 (1983).
[21] M. Hashimoto, H. Seki, and M. Yamada, Prog. Theor. Phys. **71**, 320 (1984).
[22] R. D. Williams and S. E. Koonin, Nucl. Phys. **A435**, 844 (1985).
[23] K. Oyamatsu, Nucl. Phys. **A561**, 431 (1993).
[24] C. P. Lorenz, D. G. Ravenhall, and C. J. Pethick, Phys. Rev. Lett. **70**, 379 (1993).
[25] K. S. Cheng, C. C. Yao, and Z. G. Dai, Phys. Rev. C **55**, 2092 (1997).
[26] Toshiki Maruyama, K. Niita, K. Oyamatsu, Tomoyuki Maruyama, S. Chiba, and A. Iwamoto, Phys. Rev. C **57**, 655 (1998).
[27] T. Kido, Toshiki Maruyama, K. Niita, and S. Chiba, Nucl. Phys. **A663-664**, 877 (2000).
[28] G. Watanabe, K. Iida, and K. Sato, Nucl. Phys. **A676**, 445 (2000).
[29] G. Watanabe, K. Sato, K. Yasuoka, and T. Ebisuzaki, Phys. Rev. C **66**, 012801(R) (2002).
[30] G. Watanabe and K. Iida, Phys. Rev. C **68**, 045801 (2003).
[31] C. J. Horowitz, M. A. Pérez-García, and J. Piekarewicz, Phys. Rev. C **69**, 045804 (2004).

[32] Y. Mochizuki and T. Izuyama, Astrophys. J. **440**, 263 (1995).
[33] Toshiki Maruyama, T. Tatsumi, D. N. Voskresensky, T. Tanigawa, S. Chiba, and Tomoyuki Maruyama, *Proceedings of the International Symposium on the Origin of Matter and Evolution of Galaxies 2003*, edited by M. Terasawa *et al*., (World Scientific, Singapore, 2005), p. 417.
[34] *Density Functional Theory*, edited by E. K. U. Gross and R. M. Dreizler (Plenum, New York, 1995).
[35] D. N. Voskresensky *et al*., in preparation.
[36] M. Centelles and X. Viñas, Nucl. Phys. **A563**, 173 (1993).
[37] G. Watanabe, Toshiki Maruyama, K. Sato, K. Yasuoka, and T. Ebisuzaki, Phys. Rev. Lett. **94**, 031101 (2005).